LA-UR-15-27208 (Accepted Manuscript)

Ionic Conductivity Increased by Two Orders of Magnitude in Micrometer-Thick Vertical Yttria-Stabilized ZrO Nanocomposite Films

Jia, Quanxi

To be published in: Nano Letters

DOI to publisher's version: 10.1021/acs.nanolett.5b02726

Permalink to record: http://permalink.lanl.gov/object/view?what=info:lanl-repo/lareport/LA-UR-15-27208

Ionic Conductivity Increased by Two Orders of Magnitude in Micrometer-Thick Vertical Yttria-Stabilized ZrO_2 Nanocomposite Films

Shinbuhm Lee,[†] *Wenrui Zhang,*[‡] *Fauzia Khatkhatay,*[‡] *Haiyan Wang,*[‡] *Quanxi Jia,*[§] *and Judith L. MacManus-Driscoll*[†,*]

[†]Department of Materials Science and Metallurgy, University of Cambridge, 27 Charles Babbage Road, Cambridge, CB3 0FS, United Kingdom

[‡]Department of Electrical and Computer Engineering, Texas A&M University, College Station, Texas 77843, United States

[§]Center for Integrated Nanotechnologies, Los Alamos National Laboratory, Los Alamos, New Mexico 87545, United States

KEYWORDS: ion conductivity; nanocomposite; yttria-stabilized ZrO_2; samarium-doped CeO_2

ABSTRACT

We design and create a unique cell geometry of templated micrometer-thick epitaxial nanocomposite films which contain ~20-nm diameter yttria-stabilized ZrO_2 (YSZ) nanocolumns, strain coupled to a $SrTiO_3$ matrix. The ionic conductivity of these nanocolumns is enhanced by over two orders of magnitude compared to plain YSZ films. Concomitant with the higher ionic conduction is the finding that the YSZ nanocolumns in the films have much higher crystallinity and orientation, compared to plain YSZ films. Hence, "oxygen migration highways" are formed in the desired *out-of-plane* direction. This improved structure is shown to originate from the epitaxial coupling of the YSZ nanocolumns to the $SrTiO_3$ film matrix and from nucleation of the YSZ nanocolumns on an intermediate nanocomposite base layer of highly aligned Sm-doped CeO_2 nanocolumns within the $SrTiO_3$ matrix. This intermediate layer reduces the lattice mismatch between the YSZ nanocolumns and the substrate. Vertical ionic conduction values as high as 10^{-2} $\Omega^{-1}cm^{-1}$ were demonstrated at 360 ^{o}C (300 ^{o}C lower than plain YSZ films), showing the strong practical potential of these nanostructured films for use in much lower operation temperature ionic devices.

TEXT

Oxygen vacancies in transition metal oxides have attracted renewed attention as functional ionic defects for the application of ionotronics[1–5] (ionic + electronic devices such as memristors and neuristors) and energy materials[6–9] (solid oxide fuel cells and catalysts). However, achieving high ionic conductivity at temperatures below ~650 °C in a practical way is a critical challenge.[6–8]

To achieve fast ion transport, i.e., high ionic conductivity in the well-studied ionic conductor, yttria-stabilized ZrO_2 (YSZ) multilayer films with lateral hetero-interfaces have been widely explored.[10–15] Garcia-Barriocanal *et al.* demonstrated the colossal enhancement of ionic conduction by several orders of magnitude.[10] However, these effects have only been observed in ultrathin YSZ films (1-nm-thickness) and in the *in-plane* direction,[10] thus limiting their applications potential.[7,8] In these YSZ multilayer films, it is known that there is disorder of oxygen sublattice, resulting from relaxation of lattice mismatch strain.[10–15] While this may play a role in enhancing ionic conduction,[10–15] the physical mechanisms of enhanced ionic conduction at heterointerfaces is still not fully understood.[16–21] In part, this is because in the planar multilayer film geometry, the location and extent of the ionic conduction are very hard to probe. On the other hand, it is clear that the materials combination in the heterostructure is important.[14,15] Furthermore, as pointed in a recent review,[15] the increase of ionic conductivity in the multilayer films of YSZ and $SrTiO_3$ (STO) has a large quantitative scatter from none to 10^8 times, compared with single crystalline YSZ. To overcome such ambiguous issues, to obtain a clear understanding, and to give the ability to tune and enhance the ionic conductivity, new approaches are needed.

Self-assembled nanocomposite films (hereafter termed nanoscaffold films) have recently been explored for ionotronics and for energy applications.[22–28] In these films, two epitaxial oxides phases grow vertically on a single crystal substrate. Compared with lateral multilayer films, nanoscaffold films have several relative merits. Since each layer is exposed to the surface, it is electrically addressable without destructive patterning.[24,26,27] Also, while there are a few interfaces in the lateral multilayers, there are a very large number of interfaces in the nanoscaffold films. The nanocolumns and the vertical interfaces with the matrix are well ordered and highly tunable in terms of dimensions and properties, respectively.[28] More importantly, owing to the vertical strain coupling of the two phases, the strain state is preserved in thick (above micrometer) films.[28–30] Finally, the strain state of nanocolumns and matrix can be modulated by selection of phases with the appropriate elastic moduli.[25,31] Despite the aforementioned advantages, to date, the magnitudes, precise location, origin of and tuning of ionic conduction in nanoscaffold systems have not been widely explored. This is likely because the materials combinations have not been selected to achieve very high structural perfection and alignment of the ionic nanocolumns.

Sub-nanometer-ultrathin films of YSZ (lattice constant of 5.135 Å from JCPDS #899069) grow epitaxially on STO (001) (3.905 Å from JCPDS #790174) substrates with a 45^{o} in-plane rotation to minimize the lattice mismatch.[10] Even with the 45° rotation, the lattice mismatch is still as large as 7.5 %. When thicker films are grown, namely sub-micrometer-thick, a high concentration of misfit dislocations forms to reduce the strain, and these imperfect crystalline YSZ films yield reduced oxygen vacancy migration compared to YSZ single crystals.[32,33] On the other hand, applications of YSZ in fuel cells, oxygen separation membranes, and other ionotronic devices will require thick films of several micrometer in order to give high durability and

mechanical stability as well as to eliminate any chances of porosity.[7] Hence, highly epitaxial and highly crystalline YSZ needs to be developed in micrometer-thick-films. To achieve this, the level of non-uniform strain in the films should be low and also the substrate must not deteriorate the film properties. In any planar film systems, the only route to achieving such high quality films is to grow them to be ultrathin, and to grow them on highly lattice matched substrates. However, this is obviously impractical for applications. As we show here, the double layer nanocomposite films overcome both the thickness and substrate limitations.

We fabricated and compared the properties of three different, sub-micrometer thick, YSZ-based systems, all grown on 1 % at. Nb-doped STO substrates. The first was a plain YSZ film (system I, Figure 1c), the second a YSZ-STO nanocomposite film (system II) containing YSZ nanocolumns embedded in a STO matrix, and the third a Sm-doped CeO_2 (SDC)-STO templated YSZ-STO film (system III). In latter system, SDC forms nanocolumns in the STO matrix, just as YSZ does, but the lattice mismatch of the SDC (lattice constant of SDC is 5.433 Å from JCPDS #750158)) with the STO is lower (1.6 %) compared to YSZ with STO.

We deposited double-layer YSZ-STO/SDC-STO nanoscaffold films by pulsed laser deposition. The Nb-doped STO (001) single crystals was selected as the substrate since it has been considered as a solid oxide fuel cell anode material due to redox stability and electrochemical properties.[34,35] We first grew the SDC-STO nanoscaffold films by ablating a polycrystalline target containing a 50:50 *wt.* % mix of SDC and STO. Then, we grew the YSZ-STO nanoscaffold film on it by ablating a polycrystalline target containing a 50:50 *wt.* % mix of YSZ and STO. We *in-situ* deposited both layers without breaking vacuum by rotating the target carousel to avoid contamination at the place where both layers were joined. To compare the enhancement of the cell properties, we deposited both plain single phase YSZ and STO films.

We used a KrF laser (λ = 248 nm) with a fluence of 1.5 J/cm^2 and a repetition rate of 1 Hz. The films were grown at a substrate temperature of 800 °C and an oxygen pressure of 0.2 mbar. Overall film thicknesses were in the range of 400 nm to 2 μm. The samples were post-annealed at 650 ^{o}C for 1 hour under 400 mbar O_2 to assure equilibrium oxygen stoichiometry and to minimize the creation of oxygen vacancies inside the films. Circular Pt electrodes of 50-μm radius defined by shadow masks were deposited by DC-magnetron sputtering onto the film surface. X-ray diffraction was carried out with a Panalytical Empyrean high resolution x-ray diffractometer using Cu-$K\alpha$ radiation (λ = 1.5405 Å).

The microstructural characterization was conducted using transmission electron microscopy (TEM) (FEI Tecnai G2 F20) operated at 200 kV. Cross-sectional samples for TEM were prepared by a standard manual grinding and thinning of samples with a final ion-milling step (Gatan PIPS 691 precision ion polishing system).

The transport characteristics as a function of temperature (20 to 550 ^{o}C) were measured using a probe station equipped with a hot plate and an HP 4294A Precision Impedance Analyzer. For all electrical measurements, we grounded the Nb-doped STO substrate and applied a voltage to the Pt electrodes.

The ionic conductivity σ was measured for the three different film systems. The measurement of σ is described elsewhere.[10,25,36] As shown in Figure 2a, we measured the frequency f dependence of the macroscopic ac conductivity σ_{ac} in system III in the f-range of 40-10^6 Hz with the ion blocking Pt metal electrodes.[35] Since σ_{ac} is governed by ion movements in the bulk at high frequency, σ_{ac} decreases with decreasing f.[36] The power law dependence of σ_{ac} universally merges into $\sigma_{ac} \sim f$ at high frequency. Between high and low frequencies, the σ_{ac} is independent of f-variation. The plateaus of σ_{ac} shift upwards with increase of temperature. At low

frequency, σ_{ac} decreases again with decreasing f since the electrode polarization effect is dominant near the electrodes.[36] The ions are blocked by the Pt electrodes and accumulated near the electrodes, leading to the formation of space-charge layers and rapid voltage drop in these layers. We defined σ from the plateaus of ac conductivity, as indicated by star symbols in Figure 2a.

Figure 2b shows the temperature T dependence of σ in the range of room temperature to 800 K for the different films and for nominally single crystalline YSZ reported in literature.[10] The striking observation from this plot is the very high ionic conductivity values for the nanoscaffold films (systems II and III) compared to the plain YSZ films (system I) and single crystalline YSZ. As shown in Table 1, for system III, σ reaches ~10^{-3} $\Omega^{-1}cm^{-1}$ at 520 K, while at least 780 K is required for the same σ value for system I. Compared to previous literature values for planar multilayer films including YSZ, as shown in Figure S1, our ionic conductivity value in system III is higher by 1−3 orders of magnitude, irrespective of micrometer-thick nanoscaffold film. As listed in Table 1, the activation energies decrease with increase of σ-values, i.e., system I (1.1±0.1 eV), II (1.1±0.1 eV), and III (0.7±0.1 eV), indicating that the oxygen ions can move with less resistance in system III. Also, we note that the dc conductivity values are around one order of magnitude lower than the ionic conductivity values across the whole temperature range, as shown in Figure S2, for the system III film. This proves the strong domination of ionic over electronic conduction in the YSZ/STO composite system.[10]

Compared with system I (whose values are in good agreement with other single crystalline YSZ reported previously[10]), the σ values measured for system III are enhanced by at least two orders of magnitude. The σ values for system III are also higher than those of system II, by at least one order of magnitude. System II has an ionic conductivity higher than plain YSZ

films (system I) by one order of magnitude. Hence, even for the less crystalline YSZ nanocolumns of system II than that of system III, a significant increase in ionic conductivity is still obtained compared to standard plain YSZ films. Since for system II the ionic conduction is higher than plain STO films by two orders of magnitude, we can rule out STO being the highly conducting pathway in system II. We also include in Figure 2b the σ of single-layer SDC-STO nanoscaffold films. The values for single layer SDC-STO are comparable to that of system III, indicating that the bottom SDC-STO nanocomposite layer in system III does not limit the rate of ionic transport in the top YSZ-STO layer which is connected in series.

To understand the physical origin of the enhanced σ values for systems III and II compared to system I, we undertook comparative studies of the film morphologies, crystallinity, alignment, and strain. We show that the key factors for enhancing ionic conductivity are crystallinity and alignment. We also postulate that interfacial structural mismatch effects cannot be ruled out as contributing to the enhancement of ionic conduction. We first discuss the results of the film morphology.

The nanostructure morphology of system III from TEM in Figure 3a showed that the YSZ-STO nanoscaffold film is templated on the SDC-STO nanoscaffold film. We note that this is the first time that such a double-layer nanoscaffold structure has been demonstrated. Figure 3b shows cross-sectional TEM images revealing the growth of the dark-colored nanocolumns of SDC in an STO matrix, growing all the way from the substrate, as well as nanocolumns of YSZ continuing through into the top-layer composite film, as indicated by triangles and circles. The nanocolumns are distributed with even sizes of ~20-nm-spacing and ~20-nm-diameter. The clean vertical interfaces between YSZ and STO are shown in the top and bottom images of Figure 3c. The middle image of Figure 3c shows an enlarged view of the interfacial region between the

YSZ-STO and SDC-STO. It is clear that the YSZ nanocolumns grow on the SDC nanocolumns and the top STO matrix grows on the bottom STO matrix. The YSZ more readily nucleates on SDC than on STO since it has the same fluorite crystal structure ($Fm\bar{3}m$ in the notation of the space group).[37–39] Likewise, STO nucleates and grows on STO since it is the same material. Having established the presence of very fine, highly aligned nanocolumns of YSZ in the films, we now determine the influences of their crystallinity and alignment on ionic conductivity.

Influence of Crystallinity and Structural Alignment on Ionic Conductivity

We study x-ray structural data of systems I, II, and III. Systems II and III are ideal configurations to compare since they have the same structural misfit and should have similar strain levels (as discussed below and shown in Table 1). On the other hand, they differ because they were nucleated on different substrates and hence their levels of alignment and crystallinity are likely to be different. System I is ideal to compare to the other two systems since it is a plain YSZ film without any additional vertical interface effects.

The x-ray diffractograms of Figure 4a show that all the different sample types have a dominant YSZ (00*l*) orientation with the main reflection being the (002) at $2\theta \approx 35^{o}$. However, for the plain YSZ films (system I), two peaks also appear at 30^{o} and 50^{o}, corresponding to the YSZ (111) and YSZ (022) reflections, respectively. The different orientations confirm the difficulty of achieving a single crystalline orientation when growing the fluorite YSZ phase on the perovskite STO substrate. On the other hand, for the films of systems II and III, there are only YSZ (00*l*) reflections without YSZ (111) and YSZ (022), indicating the role of the surrounding STO matrix for stabilizing the single orientation.

The ϕ-scans of the YSZ (111) and STO (111) reflections in system I (upper two plots of Figure 4b) show both the 0° and 45^o in-plane orientations of YSZ on STO, i.e., $<110>_{YSZ} \| <110>_{STO}$ and $<100>_{YSZ} \| <110>_{STO}$. For the 0° orientation, the {002} planes of the YSZ match with the {110} planes of the STO.[40] For system II, as shown in Figure 4c, only a single 0° in-plane orientation was obtained for the YSZ component of the film on the STO. This again shows the strong influence of the STO matrix on the epitaxy of the YSZ nanocolumns. Owing to the encapsulation of the YSZ nanocolumns by the STO matrix, plus the initial epitaxial growth on the substrate, 3-dimensional epitaxy occurs in the YSZ nanocolumns, which is very different from the 2-dimensional planar epitaxy in the planar film case.[41] For system III, as shown in Figure 4d, only a 45^o in-plane orientation was obtained for the YSZ phases. This is different from system II because for system III the YSZ nucleates on the SDC nanocolumns which are rotated 45° with respect to the STO substrate.

The bottom plots of Figures 4b-d show ω-scans of the YSZ (002) reflections for each film system. The very large full width at half maximum (FWHM) values of 2.2^o for the plain YSZ film (system I) can be explained by the several crystal orientations which produce a large out-of-plane tilting effect. As shown in Figures 4c and d, the FWHM decreases to 1.6° for system II and then to 0.9° for system III. The FWHM of the SDC peak is only 0.5° and is lower than for any of the YSZ peaks because it is more closely lattice matched to the STO substrate. It is clear that for system III the *in-between* lattice parameter of the SDC (it is closer to STO than YSZ is) aids the formation of highly aligned and highly crystalline YSZ nanocolumns which grow on top of it.

Figure 4e compares reciprocal space maps for the three film types. We scanned around the $(\bar{2}03)$ STO substrate peak since both the $(\bar{2}\bar{2}4)$ YSZ and $(\bar{2}\bar{2}4)$ SDC peaks have a very strong

intensity close to this peak. The quantitative peak breadths are shown in Figure 2d and Table 1. For the plain film of system I (left figure), the substrate-induced strain was fully relaxed, as would be expected for a 1-μm-thick film. A broad $(\bar{2}\bar{2}4)$ YSZ peak in q_z-axis was measured, indicating a large spread of lattice parameters as a result of the gradual strain relaxation through the film thickness. For system II (middle figure), the $(\bar{2}\bar{2}4)$ YSZ peak is narrower along the q_z-axis compared to system I, indicating a narrower spread of c-axis lattice parameter values and hence little strain relaxation through the thickness of the film. This is similar to what has been observed previously in other $SrTiO_3$-Sm_2O_3 and $BaTiO_3$-Sm_2O_3 nanoscaffold films.[24,28,30] The origin of this phenomenon is that the YSZ crystallinity is controlled by the encapsulating STO matrix rather than the substrate as is the case in a plain heteroepitaxial YSZ film. Hence, the YSZ strain state remains constant with film thickness which very unlike the case for standard planar films where strain varies with film thickness.[41] The peak q_z-position for the $(\bar{2}03)$ STO matrix is lower than that of the substrate, indicating an extended c-lattice parameter of the STO matrix, consistent with the 2θ–θ scan in Figure 4a.

Turning now to the highest ionic conductivity films of system III (right figure), it is observed that the $(\bar{2}\bar{2}4)$ YSZ and the $(\bar{2}\bar{2}4)$ SDC peaks are narrower along the q_z-axis compared to the systems I and II, and also the intensity of $(\bar{2}\bar{2}4)$ YSZ peak is much stronger than the single layer nanoscaffold film of system II. These results show the much higher crystallinity of the films of system III than system II, as a result of their close lattice match to the SDC nanocolumns on which they nucleate.

A plot of the FWHM of the YSZ RSM $(\bar{2}\bar{2}4)$ peak along q_z for the three systems is shown in Figure 2d, with the values shown in Table 1. The dependence of the σ values on the

peak widths shows a similar trend as for the FWHM of ω-scans in Figure 2c, showing again that a uniform, highly crystalline, highly aligned lattice is necessary to give enhanced ionic conduction.

In summary, as shown in Figures 2c and d and in Table 1, the FWHM values of both the ω-rocking curves and q_z-values are considerably lower in system III than in system II and both showing a close correlation to the measured σ values. Hence, it is clear that ionic conduction is enhanced by higher crystallinity, and alignment. Such a highly ordered YSZ lattice provides "oxygen migration highways"[20,21] for ionic transport.

Influence of Strain on Ionic Conductivity

The levels of strain induced in the different phases in the three film systems are given in Table 1. For the films of systems II and III, the film STO (002) reflection at $2\theta \approx 46°$ is shifted down from that of the substrate peak, indicating vertical tensile strain in the STO in the film. For systems II, the lattice constant of STO phase is elongated to 3.923 Å (tensile strain of 0.46 %, *cf.* 3.905 Å in unstrained STO phase). On the other hand, the lattice constant of the YSZ phase is decreased to 5.126 Å (compressive strain of 0.17 %, *cf.* 5.135 Å in unstrained YSZ phase). Since the Young's modulus of STO (175 GPa)[41] is comparable to that of YSZ (180 GPa),[11,13] neither phase dominates the other in terms of the vertical strain and hence both will adjust their lattice parameters to give the minimal vertical interfacial energy

For the films of system III, The STO and YSZ lattice constants of STO and YSZ are elongated to 3.917 Å (tensile strain of 0.31 %) and decreased to 5.124 Å (compressive strain of 0.21 %), respectively. The SDC (002) reflection is also observed for system III, at $2\theta \approx 33°$,

indicating the same (00l) orientation as for YSZ, as expected. The lattice constant of the SDC is decreased to 5.422 Å (compressive strain of 0.20 %, cf. 5.433 Å in unstrained SDC phase), almost similar to the YSZ strain.

Comparing film types II and III the strain levels are close in both systems, and critically, the YSZ is in compression by the STO in both film types, by 0.17 and 0.21%, respectively, i.e., to very similar levels in both systems. Since compressive strain does not enhance ionic conductivity because it leads to an increase of the oxygen vacancy migration barrier[11–15] and since the values are very close for the two systems but the ionic conductivity values are different, we rule out strain as the origin of the ionic conduction enhancement in our samples. On the other hand, we should also consider the influence of tensile strain on ionic conductivity of the STO since strain has been shown to enhance oxygen ionic conductivity in vertical and lateral multilayer systems.[10–15,25] The tensile strain reduces the activation energy for oxygen vacancy migration because the spatial volume of the moving species increases. To determine whether the tensile strain in the STO phase affects the enhancement of ionic conductivity, we consider recent calculations of how the ratio of ionic conductivities for strained and non-strained films varies with the level of epitaxial strain $\Delta a/a$. It is found that:

$$ln\left(\frac{\sigma_{strained}}{\sigma_{non-strained}}\right) \cong \frac{1}{3}\frac{\Delta V^{M}}{RT}\frac{Y}{1-\nu}\frac{\Delta a}{a} \qquad (1),$$

where a represents the lattice constant in non-strained film.[11,13,20] The Δa is defined as the difference of lattice constants for strained and non-strained films. ΔV^{M}, Y (≈175 GPa),[42] and ν (≈ 0.232)[43] represent the volume of migration of oxygen vacancies, the Young's modulus, and the Poisson ratio of STO, respectively. Although we do not know the exact ΔV^{M}-value of STO, we considered widely-studied YSZ materials ($\Delta V^{M} \approx 2.08\times10^{-6}$ m^3mol^{-1}) since its Y (≈ 180 GPa) and ν (≈ 0.3)[11,13] are similar to those of STO. In lateral multilayer films of tensile-strained YSZ,

$\frac{\sigma_{strained}}{\sigma_{non-strained}} \sim 2.7$ and ~ 16 when $\Delta a/a \cong 0.03$ and $\cong 0.06$,[11,13,20] respectively. However, the expected contribution of tensile-strained STO phase to enhancement of ionic conductivity would be negligible since $\Delta a/a \cong 0.0031$, i.e., a very low value. Hence, we can rule out strain as being a contributor to enhanced ionic conduction in our nanoscaffold films.

Influence of Space Charge Effects on Ionic Conductivity

In solid-state ionics, it is widely accepted that when two ionic conductors form an interface, a fast ionic transport pathways can be generated here due to the overlap of space charge regions.[44,45,46] Since the diameter of the YSZ nanocolumns is only ~ 20 nm, we should consider the effect of space charge regions at the YSZ/STO interfaces as the origin of high ionic conductivity. However, it is expected that the widths of the space charge regions are very narrow (below 1 nm) in the heavily doped ionic conductors such as YSZ.[47] Therefore, the space charge region cannot overlap at the vertical interfaces in YSZ-STO nanoscaffold films. It is worth noting that the additional accumulation of charge carriers at the space charge regions in the heterostructures made of heavily doped oxides cannot significantly affect the total conductivity compared with large bulk defect concentrations because the width of the space charge regions will be too small.[47] Hence, the space charge effect can also be ruled out.

Influence of the Presence of Structurally Misfit Vertical Interfaces on Ionic Conductivity

Finally, we consider whether, as well as enhanced ionic conduction along the YSZ nanocolumns arising from their high crystallinity and alignment, there is additionally enhanced ionic conduction arising from oxygen vacancies at the interfacial regions in the vertical nanoscaffolds films of systems II and III. This enhancement effect is possible if there is structural misfit between the vertical interface, which is indeed the case here owing to the STO having a perovskite structure and the YSZ having a fluorite structure.[23–27] As schematically shown in Figure 2a, there is incoherent domain matching of $2 \times (001)_{\text{STO-strained}}$ ($\approx 2 \times 3.905$ Å = 7.81 Å) $\approx 3 \times (002)_{\text{YSZ-strained}}$ ($\approx 3 \times 5.135/2$ Å = 7.71 Å). The interfacial structural modifications will not just be restricted to one or two atomic layers but will penetrate to several atomic layers, making up a reasonable fraction of the volume of the ~ 20 nm columns.[44]

In systems I and II, the σ of system II is much higher than that of system I although the activation energy is the same (to within error). Since σ is expressed as following: $\sigma = \frac{\sigma_o}{T} exp\left(-\frac{E_a}{k_B T}\right)$, where T and k_B are temperature and Boltzmann constant, respectively, higher σ indicates a higher preexponential factor σ_o. The σ_o is a materials-dependent preexponential factor, which is related to the hopping rate, the vibrational frequency of the mobile ions, the number of equivalent sites per unit volume, the concentration of mobile ions, and the entropy.[48] The constituents will be influenced by presence of the structurally misfit vertical interfaces which leads to a higher concentration of oxygen vacancies in the interfacial regions. Hence, the enhancement of ionic conductivity in system II than system I would be attributed to the increase of σ_o-values.

By comparing systems II and III which have the *same* structural misfit of the vertical hetero-interfaces (in addition to very similar strain states), we can deduce that the effect of crystallinity and alignment of the YSZ nanocolumns plays at the very least the *dominant role* in

enhancing ionic conduction. This is deduced because system III with a higher structural quality than system II has a considerably higher ionic conduction even though it contains the *same* vertical interfaces (i.e., YSZ/STO). However, we cannot rule out the additional, more minor role of interfacial structural misfit enhancement of ionic conductivity.

In conclusion, using vertical heterointerface nanocomposite films containing ~ 20-nm-diameter vertical YSZ nanocolumns, we induced ionic conductivity values which are much higher than that of plain YSZ films by at least two orders of magnitude. The optimum YSZ-based nanocomposite film was grown with very high orientation and crystallinity by seeding its growth on a sub-layer of SDC-STO nanoscaffold film, which grows highly aligned and epitaxially on STO because of the closer lattice match of SDC to STO than YSZ to STO.

The unique nanoscaffold geometry enabled the origin strong enhancement in ionic conduction in the YSZ to be elucidated: it arises because the nanoscaffold system gives highly aligned, highly crystalline material which cannot be achieved in standard planar films unless they are grown to be *ultrathin* (< 1 nm). Additional enhancement of ionic conduction due to oxygen vacancies formed near structurally misfit vertical hetero-interfaces between the STO matrix and the YSZ nanocolumns is also a possibility in this system but it appears to be not the major contributory factor.

Compared to earlier work where high ionic conductivity was accomplished only in ultrathin films, here we achieved high ionic conductivity in micrometer-thick films. These self-assembled films are much more practical for the development of low temperature solid oxide fuel cells, first because the ions travel in the necessary out-of-plane direction, second because

their larger thickness means they are rigid and dense, and third because they have the possibility to be grown by rapid deposition routes.[49]

Supporting Information

Figure S1 and Figure S2. These materials are available free of charge via the Internet at http://pubs.acs.org.

Corresponding Author

*E-mail: jld35@cam.ac.uk

Author Contributions

S.L. and J.L.M.-D. conceived the project and directed the research. S.L. grew samples and performed x-ray diffraction and transport measurements. W.Z., F.K., and H.W. carried out TEM measurements. Q.X.J discussed the results with valuable comments. S.L. and J.L.M.-D; wrote the paper. All authors discussed the results fully and commented on the manuscript.

Funding Sources

This work was supported by the European Research Council (ERC) (Advanced Investigator grant ERC-2009-AdG-247276-NOVOX), the UK Engineering and Physical Sciences Research Council (EPSRC) and the U.S. National Science Foundation (grant no. DMR-1401266). The work at Los Alamos was partially supported by the NNSA's Laboratory Directed

Research and Development Program and was performed, in part, at the Center for Integrated Nanotechnologies, an Office of Science User Facility operated for the U.S. Department of Energy (DOE) Office of Science.

REFERENCES

1. Kalinin, S. V.; Spaldin, N. A. Functional Ion Defects in Transition Metal Oxides. *Science* **2013**, *341*, 858–859.

2. Yang, C.-H.; Seidel, J.; Kim, S. Y.; Rossen, P. B.; Yu, P.; Gajek, M.; Chu, Y. H.; Martin L. W.; Holcomb, M. B.; He, Q. *et al.* Electric Modulation of Conduction in Multiferroic Ca-Doped $BiFeO_3$ Films. *Nature Mater.* **2009**, *8*, 485–493.

3. Waser, R.; Dittmann, R.; Staikov, G.; Szot, K. Redox-Based Resistive Switching Memories – Nanoionic Mechanisms, Prospects, and Challenges. *Adv. Mater.* **2009**, *21*, 2632–2663.

4. Strukov, D. B.; Snider, G. S.; Stewart, D. R.; Williams, R. S. The Missing Memristor Found. *Nature* **2008**, *453*, 80–83.

5. Yang, J. J.; Strukov, D. B.; Stewart, D. R. Memristive Devices for Computing. *Nature Nanotech.* **2013**, *8*, 13–24.

6. Skinner, S. J.; Kilner, J. A. Oxygen Ion Conductors. *Mater. Today* **2003,** *6,* 30–37.

7. Wachsman, E. D.; Lee, K. T. Lowering The Temperature of Solid Oxide Fuel Cells. *Science* **2011**, *334*, 935–939.

8. Wachsman, E.; Ishihara, T.; Kilner, J. Low-Temperature Solid-Oxide Fuel Cells. *MRS Bull.* **2014,** *39*, 773–779.

9. Jeen, H.; Choi, W. S.; Biegalski, M. D.; Folkman, C. M.; Tung, I-C.; Fong, D. D.; Freeland, J. W.; Shin, D.; Ohta, H.; Chisholm, M. F. *et al.* Reversible redox reactions in an epitaxially stabilized $SrCoO_x$ oxygen sponge. *Nature Mater.* **2013**, *12*, 1057–1063.

10. Garcia-Barriocanal, J.; Rivera-Calzada, A.; Varela, M.; Sefrioui, Z.; Iborra, E.; Leon, C.; Pennycook, S. J.; Santamaria, J. Colossal Ionic Conductivity at Interfaces of Epitaxial ZrO_2:Y_2O_3/$SrTiO_3$ Heterostructures. *Science* **2008,** *321,* 676–680.

11. Schichtel, N.; Korte, C.; Hesse, D.; Janeka, J. Elastic Strain at Interfaces and Its Influence on Ionic Conductivity in Nanoscaled Solid Electrolyte Thin Films—Theoretical Considerations and Experimental Studies. *Phys. Chem. Chem. Phys.* **2009,** *11,* 3043–3048.

12. Schichtel, N.; Korte, C.; Hesse, D.; Zakharov, N.; Butz, B.; Gerthsen, D.; Janek, J. On The Influence of Strain on Ion Transport: Microstructure and Ionic Conductivity of Nanoscale YSZ|Sc_2O_3 Multilayers. *Phys. Chem. Chem. Phys.* **2010,** *12,* 14596–14608.

13. Korte, C.; Keppner, J.; Peters, A.; Schichtel, N.; Aydin, H.; Janek, J. Coherency Strain and Its Effect on Ionic Conductivity and Diffusion in Solid Electrolytes – An Improved Model for Nanocrystalline Thin Films and A Review of Experimental Data. *Phys. Chem. Chem. Phys.* **2014,** *16*, 24575–24591.

14. Leon, C.; Santamaria, J.; Boukamp, B. A. Oxide Interfaces with Enhanced Ion Conductivity. *MRS Bull.* **2013,** *38,* 1056–1063.

15. Yildiz, B. "Stretching" the Energy Landscape of Oxides—Effects on Electrocatalysis and Diffusion. *MRS Bull.* **2014,** *39,* 147–156.

16. Guo, X. Comment on "Colossal Ionic Conductivity at Interfaces of Epitaxial ZrO_2:Y_2O_3/$SrTiO_3$ Heterostructures" *Science* **2009,** *324,* 465a.

17. Garcia-Barriocanal, J.; Rivera-Calzada, A.; Varela, M.; Sefrioui, Z.; Iborra, E.; Leon, C.; Pennycook, S. J.; Santamaria, J. Response to Comment on "Colossal Ionic Conductivity at Interfaces of Epitaxial ZrO_2:Y_2O_3/$SrTiO_3$ Heterostructures" *Science* **2009,** *324,* 465b.

18. De Souza, R. A.; Ramadan, A. H. H. Ionic Conduction in The $SrTiO_3$|YSZ|$SrTiO_3$ Heterostructure. *Phys. Chem. Chem. Phys.* **2013,** *15,* 4505–4509.

19. Cavallaro, A.; Burriel, M.; Roqueta, J.; Apostolidis, A.; Bernardi, A.; Tarancón, A.; Srinivasan, R.; Cook, S. N.; Fraser, H. L.; Kilner, J. A. *et al.* Electronic Nature of The Enhanced Conductivity in YSZ-STO Multilayers Deposited by PLD. *Solid State Ionics* **2010,** *181,* 592–601.

20. Sanna, S.; Esposito, V.; Tebano, A.; Licoccia, S.; Traversa, E.; Balestrino, G. Enhancement of Ionic Conductivity in Sm-Doped Ceria/Yttria-Stabilized Zirconia Heteroepitaxial Structures. *Small* **2010,** *6,* 1863–1867.

21. Pergolesi, D.; Fabbri, E.; Cook, S. N.; Roddatis, V.; Traversa, E.; Kilner, J. A. Tensile Lattice Distortion Does Not Affect Oxygen Transport in Yttria-Stabilized Zirconia–CeO_2 Heterointerfaces. *ACS Nano* **2012,** *6,* 10524–10534.

22. Yoon, J.; Cho, S.; Kim, J.-H.; Lee, J.; Bi, Z.; Serquis, A.; Zhang, X.; Manthiram, A.; Wang, H. Vertically Aligned Nanocomposite Thin Films as a Cathode/Electrolyte Interface Layer for Thin-Film Solid Oxide Fuel Cells. *Adv. Funct. Mater.* **2009,** *19,* 3868–3873.

23. Su, Q.; Yoon, D.; Chen, A.; Khatkhatay, F.; Manthiram, A.; Wang, H. Vertically Aligned Nanocomposite Electrolytes with Superior Out-of-Plane Ionic Conductivity for Solid Oxide Fuel Cells. *J. Power Sources* **2013,** *242,* 455–463.

24. Lee, S.; Sangle, A.; Lu, P.; Chen, A.; Zhang, W.; Lee, J. S.; Wang, H.; Jia, Q. X.; MacManus-Driscoll, J. L. Novel Electroforming-Free Nanoscaffold Memristor with Very High Uniformity, Tunability, and Density. *Adv. Mater.* **2014,** *26,* 6284–6289.

25. Lee, S.; Zhang, W.; Khatkhatay, F.; Jia, Q. X.; Wang, H.; MacManus-Driscoll, J. L. Strain Tuning and Strong Enhancement of Ionic Conductivity in $SrZrO_3$–RE_2O_3 (RE = Sm, Eu, Gd, Dy, and Er) Nanocomposite Films. *Adv. Funct. Mater.* **2015,** *25,* 4328–4333.

26. Hsieh, Y.-H.; Liou, J.-M.; Huang, B.-C.; Liang, C.-W.; He, Q.; Zhan, Q.; Chiu, Y.-P.; Chen, Y.-C.; Chu, Y.-H. Local Conduction at the $BiFeO_3$-$CoFe_2O_4$ Tubular Oxide Interface. *Adv. Mater.* **2012,** *24,* 4564–4568.

27. Hsieh, Y.-H.; Strelcov, E.; Liou, J.-M.; Shen, C.-Y.; Chen, Y.-C.; Kalinin, S. V.; Chu, Y.-H. Electrical Modulation of the Local Conduction at Oxide Tubular Interfaces. *ACS Nano* **2013,** *7,* 8627–8633.

28. Lee, O. J.; Harrington, S. A.; Kursumovic, A.; Defay, E.; Wang, H.; Bi, Z.; Tsai, C.-F.; Yan, L.; Jia, Q. X.; MacManus-Driscoll, J. L. Extremely High Tunability and Low Loss in Nanoscaffold Ferroelectric Films. *Nano Lett.* **2012,** *12,* 4311–4317.

29. MacManus-Driscoll, J. L.; Zerrer, P.; Wang, H.; Yang, H.; Yoon, J.; Fouchet, A.; Yu, R.; Blamire, M. G.; Jia, Q. X. Strain Control and Spontaneous Phase Ordering in Vertical Nanocomposite Heteroepitaxial Thin Films. *Nature Mater.* **2008,** *7,* 314–320.

30. Harrington, S. A.; Zhai, J.; Denev, S.; Gopalan, V.; Wang, H.; Bi, Z.; Redfern, S. A. T.; Baek, S.-H.; Bark, C. W.; Eom, C.-B. *et al.* Thick Lead-Free Ferroelectric Films with High Curie Temperatures Through Nanocomposite-Induced Strain. *Nature Nanotech.* **2011,** *6,* 491–495.

31. Fouchet, A.; Wang, H.; Yang, H.; Yoon, J.; Jia, Q. X,; MacManus-Driscoll, J. L. Spontaneous Ordering, Strain Control, and Multifunctionality in Vertical Nanocomposite Heteroepitaxial Films. *IEEE Trans. Ultrason., Ferroelectr., Freq. Control* **2009,** *56,* 1534–1538.

32. Hui, S.; Roller, J.; Yick, S.; Zhang, X.; Decès-Petit, C.; Xie, Y.; Maric, R.; Ghosh, D. A Brief Review of The Ionic Conductivity Enhancement for Selected Oxide Electrolytes. *J. Power Sources* **2007,** *172,* 493–502.

33. Sun, L.; Marrocchelli, D.; Yildiz, B. Edge Dislocation Slows Down Oxide Ion Diffusion in Doped CeO_2 by Segregation of Charged Defects. *Nat. Commun.* **2015,** *6,* 6294.

34. Guo, X.; Maier, Ionically Conducting Two-Dimensional Heterostructures. J. *Adv. Mater.* **2009,** *21,* 2619–2631.

35. Blennow, P.; Hansen, K. K.; Wallenberg, L. R.; Mogensen, M. Electrochemical Characterization and Redox Behavior of Nb-Doped $SrTiO_3$. *Solid State Ionics* **2009,** *180,* 63–70.

36. Dyre, J. C.; Maass, P.; Roling, B.; Sidebottom, D. L. Fundamental Questions Relating to Ion Conduction in Disordered Solids. *Rep. Prog. Phys.* **2009,** *72,* 046501.

37. MacManus-Driscoll, J. L. Self-Assembled Heteroepitaxial Oxide Nanocomposite Thin Film Structures: Designing Interface-Induced Functionality in Electronic Materials. *Adv. Funct. Mater.* **2010,** *20,* 2035–2045.

38. Chen, A.; Bi, Z.; Jia, Q. X.; MacManus-Driscoll, J. L.; Wang, H. Microstructure, Vertical Strain Control and Tunable Functionalities in Self-Assembled, Vertically Aligned Nanocomposite Thin Films. *Acta Mater.* **2013,** *61,* 2783–2792.

39. Zheng, H., Straub, F., Zhan, Q., Yang, P.-L., Hsieh, W.-K., Zavaliche, F., Chu, Y.-H., Dahmen, U., Ramesh, R. Self-Assembled Growth of $BiFeO_3$–$CoFe_2O_4$ Nanostructures. *Adv. Mater.* **2006,** *18,* 2747–2752.

40. Kim, Y. J.; Gao, Y.; Herman, G. S.; Thevuthasan, S.; Jiang, W.; McCready, D. E.; Chambers, S. A. Growth and Structure of Epitaxial CeO_2 by Oxygen-Plasma-Assisted Molecular Beam Epitaxy. *J. Vac. Sci. Technol. A* **1999,** *17,* 926.

41. MacManus-Driscoll, J. L.; Suwardi, A.; Kursumovic, A.; Bi, Z.; Tsai, C.-F.; Wang, H.; Jia, Q. X.; Lee, O. J. New Strain States and Radical Property Tuning of Metal Oxides Using A Nanocomposite Thin Film Approach. *APL Mater.* **2015,** 3, 062507.

42. Piskunov, S.; Heifets, E.; Eglitis, R. I.; Borstel, G. Bulk Properties and Electronic Structure of $SrTiO_3$, $BaTiO_3$, $PbTiO_3$ Perovskites: An Ab Initio HF/DFT Study. *Comput. Mater. Sci.* **2004,** *29,* 165–178.

43. Ledbetter, H.; Lei, M.; Kim, S. Elastic Constants, Debye Temperatures, and Electron-Phonon Parameters of Superconducting Cuprates and Related Oxides. *Phase Trans. B* **1990,** *23,* 61–70.

44. Maier, J. Nanoionics: Ion Transport and Electrochemical Storage in Confined Systems. *Nature Mater.* **2005,** *4,* 805–815.

45. Maier, J. Ionic Conduction in Space Charge Regions. *Prog. Solid State Chem.* **1995,** *23,* 171.

46. Sata, N.; Eberman, K.; Eberl, K.; Maier., J. Mesoscopic Fast Ion Conduction in Nanometre-Scale Planar Heterostructures. *Nature* **2000,** *408,* 946.

47. Emiliana, F.; Daniele, P.; Enrico. T. Ionic Conductivity in Oxide Heterostructures: The Role of Interfaces. *Sci. Technol. Adv. Mater.* **2010,** *11,* 054503.

48. Almond, D. P.; Duncan, G. K.; West A. R. The determination of hopping rates and carrier concentrations in ionic conductors by a new analysis of ac conductivity. *Solid State Ionics* **1983,** *8,* 159.

49. MacManus-Driscoll, J. L.; Bianchetti, M.; Kursumovic, A.; Kim, G.; Jo, W.; Wang, H.; Lee, J. H.; Hong, G. W.; Moon S. H. Strong Pinning in Very Fast Grown Reactive Co-Evaporated $GdBa_2Cu_3O_7$ Coated Conductors. *APL Mater.* **2014,** *2,* 086103.

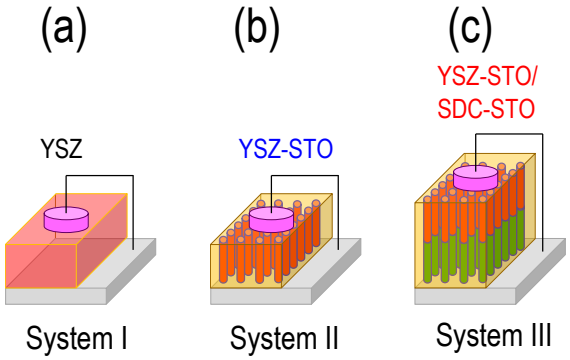

Figure 1. Schematics of (a) plain YSZ film (system I), (b) single-layer YSZ-STO nanoscaffold film (system II), and (c) double-layer YSZ-STO/SDC-STO nanoscaffold film (system III).

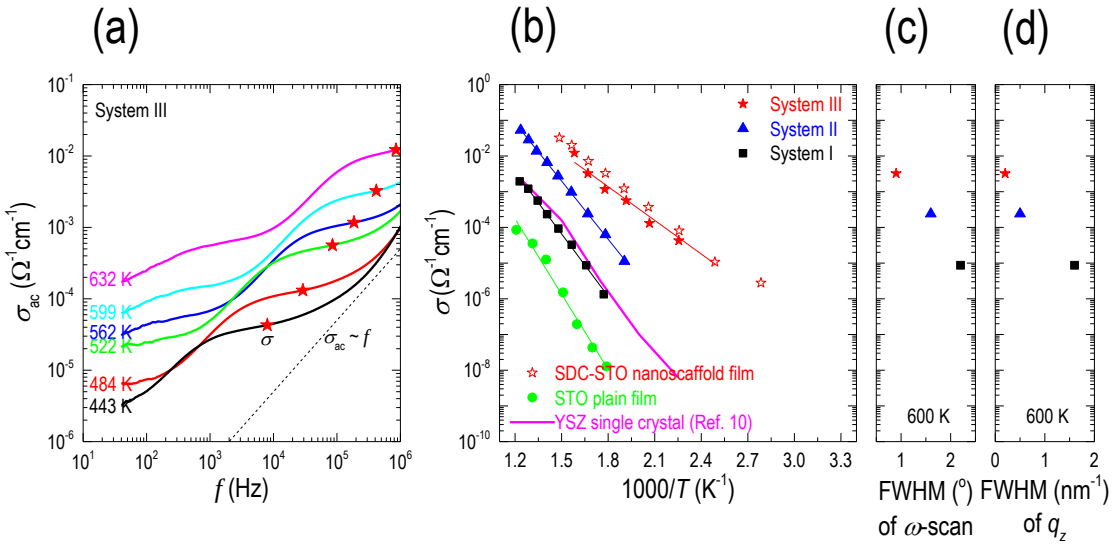

Figure 2. (a) Frequency dependence of ac conductivity σ_{ac} in system III. (b) Enhancement of ion transport in double-layer YSZ-STO/SDC-STO nanoscaffold film**.** For comparison, we also include temperature dependence of σ in YSZ-STO nanoscaffold film (system II), plain YSZ films (system I), SDC-STO nanoscaffold film, single crystalline YSZ,[10] and plain STO films. Ionic conductivity dependence of crystallinity, represented by FWHM of (c) ω-scan and (d) q_z, respectively.

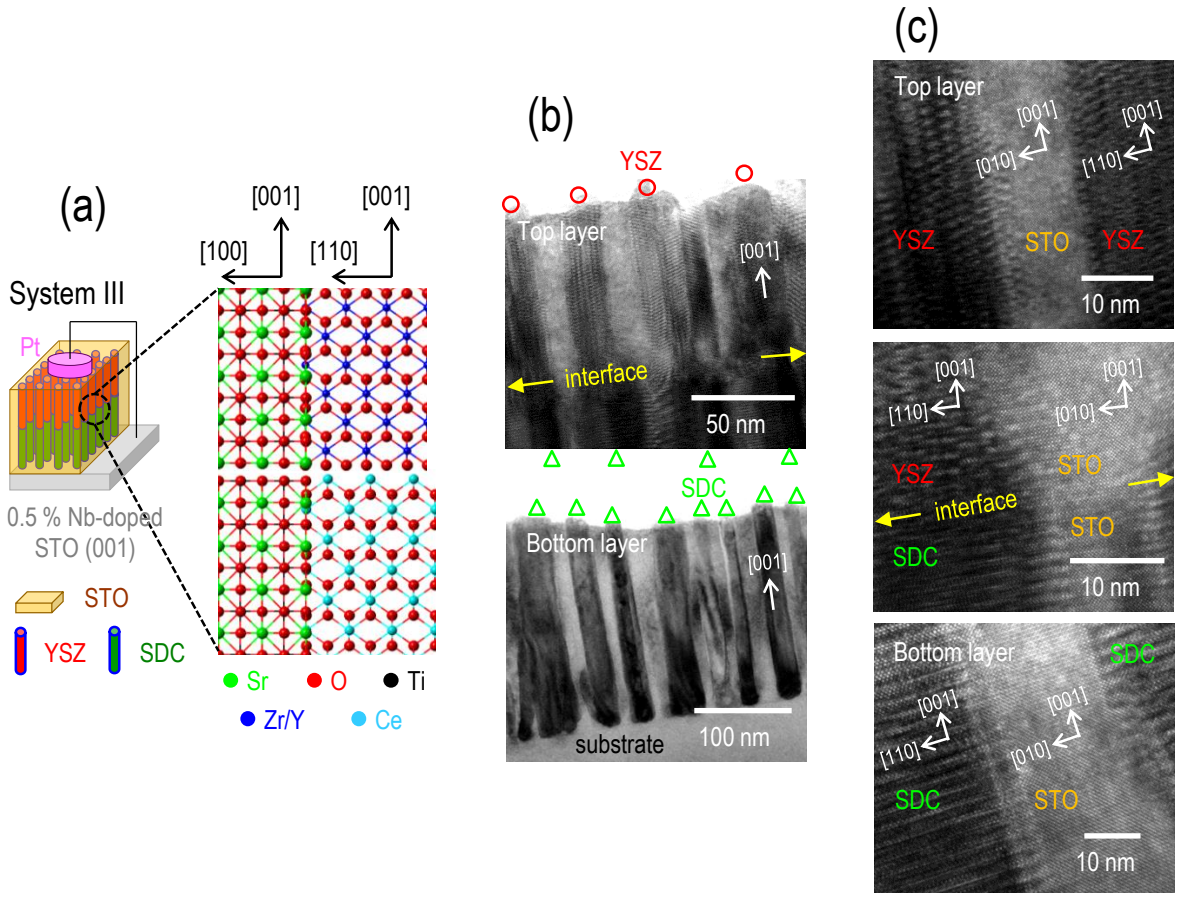

Figure 3. Cross-section of double-layer YSZ-STO/SDC-STO nanoscaffold film. (a) Schematic of self-templated nanoscafold film proposed in this work. (b) "Nano-comb"-like spontaneous phase ordering in cross-sectional view of YSZ-STO (top layer) and SDC-STO (bottom layer) in nanoscaffold film, as revealed by cross-sectional TEM image. (c) High-resolution HAADF image of vertical YSZ-STO interface (top), bordering area (middle), and SDC/STO interfaces (bottom) in cross-sectional-view.

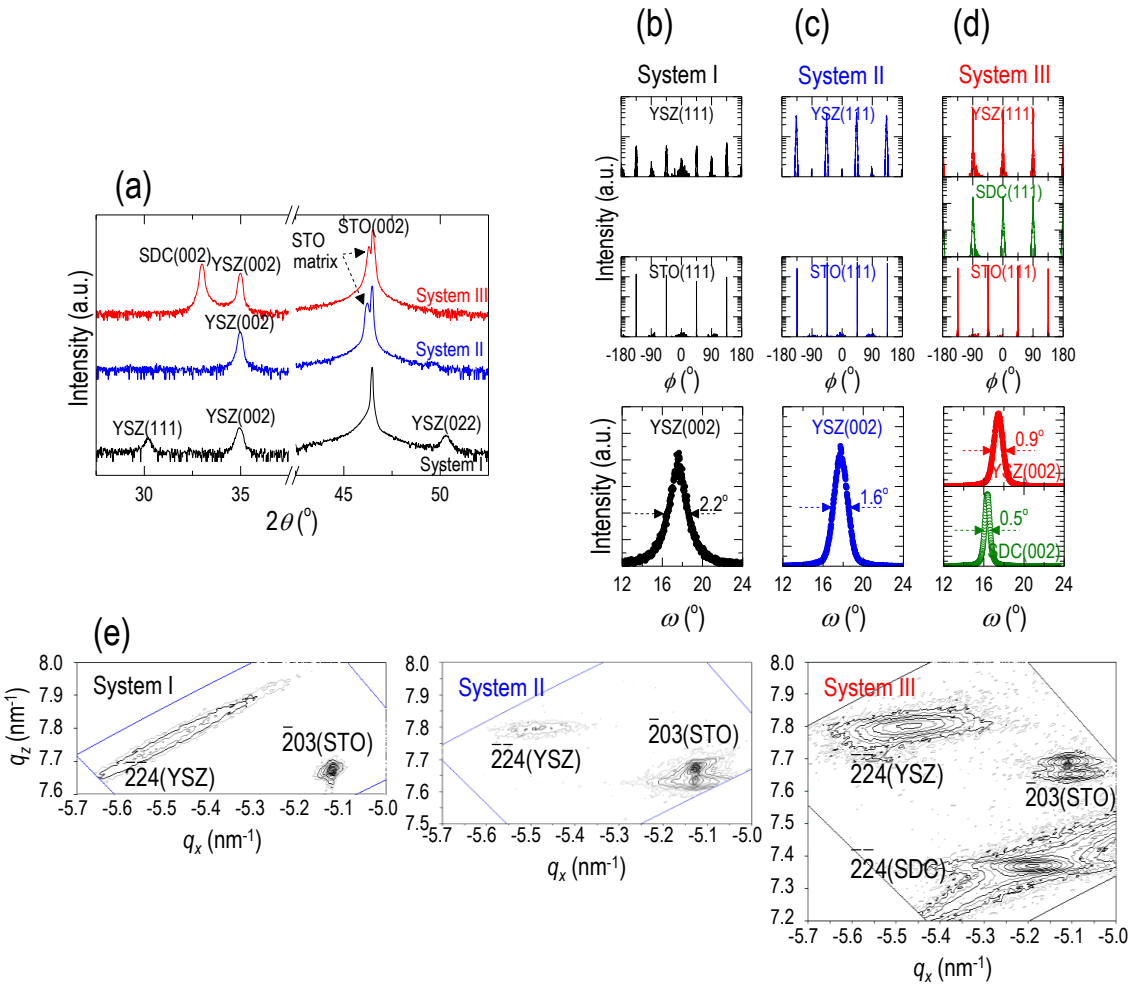

Figure 4. Crystal structure of double-layer YSZ-STO/SDC-STO nanoscaffold film. (a) Out-of-plane epitaxial relationship of double-layer YSZ-STO/SDC-STO nanoscaffold film (red line), YSZ-STO nanoscaffold film (blue line), and YSZ film (black line), investigated in 2θ–θ scan by x-ray diffraction. Investigation of ϕ-scan and ω-scan for (b) YSZ film, (c) YSZ-STO nanoscaffold film, and (d) double-layer YSZ-STO/SDC-STO nanoscaffold film. (e) Reciprocal space maps about the $(\bar{2}03)$ STO substrate for plain YSZ film, YSZ-STO nanoscaffold film, and double-layer YSZ-STO/SDC-STO nanoscaffold film.

Table 1. Summary of physical properties of systems I, II, and III.

System	Film structure	T (K) for 10^{-3} ($\Omega^{-1}cm^{-1}$)	Activation energy (eV)	Strain state	FWHM from YSZ	
					ω (^{o})	q_z (nm^{-1})
I	YSZ plain	780	1.1±0.1		2.2	1.6
II	YSZ-STO nanoscaffold	640	1.1±0.1	YSZ: 0.17 % compressive STO: 0.46 % tensile	1.6	0.5
III	YSZ-STO/SDC-STO double-layered nanoscaffold	520	0.7±0.1	YSZ: 0.21 % compressive SDC: 0.20 % compressive STO: 0.31 % tensile	0.9	0.2

Insert Table of Contents Graphic and Synopsis Here.